17
Investigating the Molecular Specific Interactions on Cell Surface Using Atomic Force Microscopy

Mi Li, Lianqing Liu, Ning Xi, and Yuechao Wang

17.1
Background

Cancer is the leading cause of death in economically developed countries and the second leading cause of death in developing countries [1]. The new cancer cases will increase from 12.7 million in 2008 to 22.2 million by 2030, while the cancer-related deaths will increase from 7.6 million in 2008 to 13.2 million by 2030 [2]. Carcinogenesis and tumor progression are complex and progressive processes that are associated with numerous genetic and epigenetic alterations [3]. Our growing understanding of tumor biology and genomics paves the way to the development of new therapy approaches, and marked progress has been achieved in overcoming treatment resistance through precision medicine and immunotherapy [4]. However, because of the fact that the exact reason why a cell becomes cancerous is unknown (the only one cancer whose cause is clear is cervical cancer), the current cancer treatments cannot prevent the recurrence of cancers and the age-adjusted mortality rate for cancer is about the same in the twenty-first century as it was 50 years ago [5].

Lymphomas, solid tumors of the immune system [6], account for 4%–5% of all cancers [7]. Hodgkin's lymphoma accounts for about 10% of all lymphomas and the remaining 90% are referred to as *non-Hodgkin lymphoma* (*NHL*) [6]. NHL can be divided into many subtypes according to the combination of morphology, immunophenotype, genetic, molecular, and clinical features of the tumors [8]. Approximately, 85% of NHL in adults arises from B cells [9], and the rest are T-cell origin [10]. Follicular lymphoma and diffuse large B-cell lymphoma are the two most common B-cell NHLs, comprising 60% of new B-cell NHL diagnoses each year in North America [11]. In 1997, US Food and Drug Administration (FDA) approved rituximab (an anti-CD20 monoclonal antibody (mAb)) for treating B-cell NHLs. CD20 is 297 amino acids long with a molecule weight of about 33 kDa [12]. The exact biological function of CD20 is currently unknown [13], partly because it has no known natural ligand and CD20 knockout mice display an almost normal phenotype [14]. Many of the functions of CD20 have been determined using artificial ligands (antibody) [15]. *In vitro* experiments proposed that CD20

Micro- and Nanomanipulation Tools, First Edition. Edited by Yu Sun and Xinyu Liu.
© 2015 Wiley-VCH Verlag GmbH & Co. KGaA. Published 2015 by Wiley-VCH Verlag GmbH & Co. KGaA.

itself functioned as a calcium ion channel, although direct evidence was lacking [16]. CD20 is an ideal target for mAbs, as it is expressed at high levels on most tumor B cells, but does not become internalized or shed from the plasma membrane after being bound by mAb [17]. Besides, CD20 is absent from hematopoietic stem cells, thus normal B cells are able to regenerate after the rituximab treatment and return to pretreatment levels within several months or even years [18].

In vitro research works have proved that the binding of rituximab to CD20 causes the death of B cells through three mechanisms, including antibody-dependent cellular cytotoxicity (ADCC), complement-dependent cytotoxicity (CDC), and direct induction of programmed cell death (PCD) [19]. While it is widely accepted that ADCC is critical in the killing effect of rituximab, the role of CDC and PCD is still disputed [20]. The schematic diagram of ADCC mechanism is shown in Figure 17.1. During the ADCC, the Fab portion of rituximab binds to CD20 on the surface of tumor cells, and then the Fc portion of rituximab binds to the Fc receptor (FcR) on the surface of immune cells (e.g., macrophage and Natural killer [NK] cell), which triggers the effector functions of immune cells. The macrophage kills the tumor cell via phagocytosis, while the NK cell releases perforin and granzymes that can lyse the tumor cell [21]. The exact contribution of macrophage and NK cell *in vivo* is so far still unclear [17]. Current research about rituximab's killing effects were virtually performed *in vitro*, thus the *in vivo* mechanisms are yet to be elucidated [19]. Even though its *in vivo* mechanism is unclear, rituximab has proven to be very effective in clinical practice either by itself or when combined with chemotherapy (such as Cyclophosphamide-Hydroxydaunorubicin- Oncovin- Prednisone [CHOP]), significantly improving the response rates and survival outcomes of B-cell NHL patients [22]. Rituximab with the standard dose of 375 mg m^{-2} [23] has been widely accepted in the clinical treatment of B-cell NHLs.

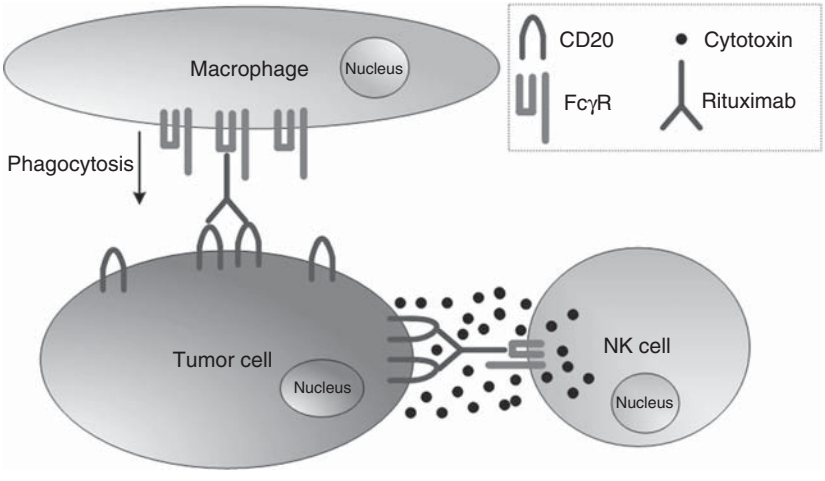

Figure 17.1 The ADCC mechanism of rituximab.

Despite the fact that rituximab achieved unprecedented success in clinical treatments, there are still about 40%–50% of patients who have no responses or develop resistance to the rituximab therapy [24]. Several new antibodies with enhanced effector functions demonstrated that *in vitro* tests have been developed (e.g., Ofatumumab, Ocrelizumab, Veltuzumab, AME-133V, PRO131921 and GA101) [23], but to date their clinical performances are disappointed in direct comparison with rituximab [25], and whether such new antibodies will be clinically superior to rituximab therapy remains to be seen [26]. In recent years, requirements for developing new antibodies to provide effective therapies for those patients who are insensitive or develop resistance to rituximab are increasingly urgent [23]. Addressing the problem of rituximab's variable efficacies among different patients will greatly promote the development of new antibody drugs and thus will improve the quality of life patients.

To further enhance the potency of anti-CD20 mAbs beyond that achieved with rituximab, it is becoming increasingly important for us to develop closer links between the laboratory and the clinic [23]. To obtain closer links, two aspects of current biochemical experiments need improvement. The first aspect is that traditional biochemical experiments are based on bulk averaging experiments that hide the behavior of single cells and single molecules [27]. For a better understanding of the underlying mechanisms of cellular physiological activities, single-cell and single-molecule experiments are required to obtain complementary information to that from bulk experiments. The second aspect needing improvement is that most current experiments were carried out on cells cultured *in vitro*. We know that the growth environment of cells cultured *in vitro* was quite different from the environment of cells *in vivo* [28]. For cells cultured *in vitro*, they lose the neurohumoral regulation and cell–cell influence, and this huge difference of growth environment may cause the changes of the cell structures and functions. Hence, the experimental results obtained from cells cultured *in vitro* may not completely reflect the real situation *in vivo*. So far the knowledge of rituximab's *in vivo* mechanisms is very scarce, greatly hindering the development of anti-CD20 mAbs. In order to develop new anti-CD20 mAbs with enhanced efficacy, we should have a thorough understanding of the physiological activities involved in rituximab's killing mechanisms, particularly the activities *in vivo*. Viewed from this aspect, directly investigating the behavior of tumor cells from B-cell NHL patients will be of significant clinical impact.

The advent of atomic force microscopy (AFM) [29] provides a powerful platform for investigating the cellular behavior at single-cell and single-molecule levels. Compared with other biochemical methods, AFM has several unique advantages. First, it has nanometer spatial resolution and can work in liquids that enable it to observe the activities of single molecules on the surface of living cells. We know that optical microscopy cannot reveal the activities of single molecules due to the 200-nm resolution limitation, and electron microscopy can only observe the behavior of chemically fixed and dried samples. Second, while chemical (fluorescence) labeling of proteins might change their surface characteristics so that their

natural activity is impaired [30], AFM is label-free and noninvasive. Third, AFM can obtain multiple complementary parameters of the biological systems (from single molecules to cells and tissues), for example, topography, adhesion, elasticity, and dissipation [31]. These parameters are of great significance for us to understand the underlying mechanisms of biological systems. These advantages have made AFM widely used in the life sciences in the past decades.

In this chapter, we describe the application of AFM in investigating the molecular specific interactions involved in rituximab targeted therapy of lymphoma on cell surface. The structure of this chapter is as follows. We begin by providing an introduction about the principle and method of AFM single-molecule force spectroscopy (SMFS), a technique that can probe the molecular interactions at single-molecule levels. In the next section, we discuss how to measure the drug–target interactions directly on tumor cells from lymphoma patients. Next, investigations about mapping the nanoscale distribution of target proteins on the surface of tumor cells are presented and the relationship between the distribution of target protein and the clinical rituximab efficacy is analyzed. The last section is the summary.

17.2 Single-Molecule Force Spectroscopy

SMFS specifically probes the membrane proteins by linking their cognate ligands to the AFM tip, as depicted in Figure 17.2a. With the ligands on the AFM tip that can bind to the specific membrane proteins, one can localize, detect, and manipulate the membrane proteins on the living cell [27]. An AFM cantilever has one end fixed to a piezoelectric ceramic driver, and the free end has a sharp tip. The vertical movement of the probe is driven by a piezoelectric ceramic, and any deformation of the cantilever due to repulsive or attractive forces is monitored by a four-quadrant photodetector that senses laser light reflected from the back of the cantilever. According to Hooke's law ($F = kx$), if the spring constant k and the deformation x of the cantilever are known, then the force F applied to the cantilever can be computed. The vertical displacement of the probe is obtained from the piezoelectric ceramic driver. In the force curve mode, the tip gradually approaches and contacts the cell such that the ligands bind to the membrane proteins. Then, the tip is retracted from the cell surface. After recording the displacement of the driver and the force on the cantilever during the approach–retract cycle, a force versus distance curve (also called *force curve*) is obtained, as shown in Figure 17.2b. The arrows indicate the process of obtaining the force curve. When the tip does not contact the cell, the cantilever remains unchanged and the force curve is flat (Figure 17.2b(I)). After contacting the cell, the cantilever is deformed (bent) and the force curve becomes bent (Figure 17.2b(II)). If the ligands on the AFM tip bind to the membrane proteins during the contact between AFM tip and cell surface, then the protein–ligand pair is stretched when the tip is retracted (Figure 17.2b(III)). When the pulling

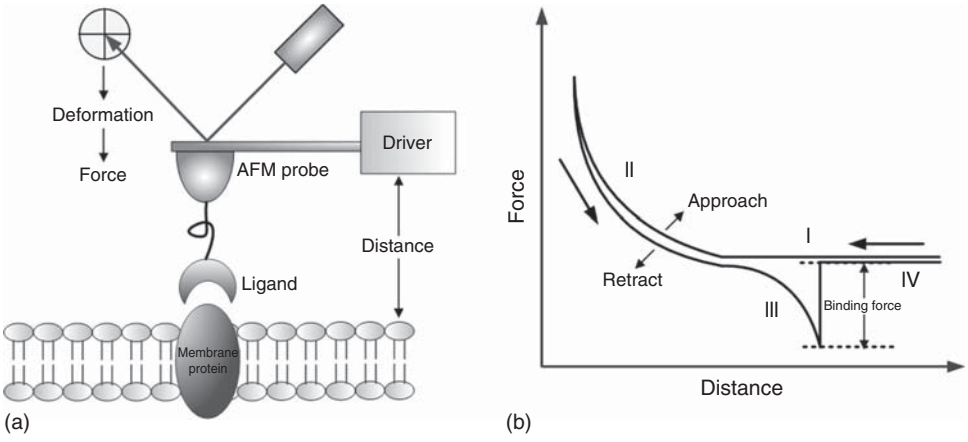

Figure 17.2 Principle of SMFS. (a) Ligands attached to an AFM tip probe a membrane protein. (b) Example of a force curve. When the cantilever/tip is far away from the cell, no deformation occurs, creating a flat force curve (I). After the tip contacts the cell, cantilever deformation occurs and the force curve becomes curved (II). When the tip retracts, the protein–ligand bond is stretched until it ruptures (III). The tip finally retracts to the original position (IV). (Reprinted with permission from Ref. [32]. Copyright 2014 Science China Press.)

force exerted by the cantilever becomes larger than the binding force of the protein–ligand pair, then the protein–ligand bond ruptures and a specific unbinding jump appears in the retraction curve. The magnitude of the jump (denoted by the double-head arrow in Figure 17.2b) corresponds to the binding force between membrane protein and ligand. Then the tip retracts to its original position, as shown in Figure 17.2b(IV).

The prerequisite for using SMFS to measure molecular binding forces is the linking of ligands onto the AFM tip, which is called *tip functionalization*. There are three main methods for tip functionalization, including protein physisorption, chemisorption of alkanethiols on gold, and covalent coupling of silanes on silicon oxide [33]. The major drawback of protein physisorption is that it often exhibits many molecular binding events during the measurement and it is therefore difficult to accurately measure the binding force of a single molecular pair [34]. The disadvantage of alkanethiol chemisorption is that it requires the tip to be coated with a 5-nm-thick chromium layer, followed by a 30-nm-thick gold layer [35]. This causes a significant increase in the tip radius that decreases the spatial resolution during scanning [36]. The covalent coupling method can be performed directly on a silicon tip, and the binding strength of a covalent bond is much stronger than that of physisorption or chemisorption [37, 38]. Therefore, this method is very well suited for molecular force measurement. During covalent coupling, a silicon tip is first coated with NH_2, and then the ligands are linked onto the tip via hetero-bifunctional polyethylene glycol (PEG) molecules (e.g., NHS–PEG–PDP [33]). The NHS end of the PEG linker covalently binds to the

NH_2 on the tip surface, and the PDP end forms covalent disulfide bonds to SH groups on the ligands. Most extracellular proteins (such as antibodies) do not have SH groups; however, they can be formed with *N*-succinimidyl 3-(acetylthio) propionate (SATP) [39]. The insertion of a PEG spacer between the ligand and the tip has many advantages. It allows the ligand to freely reorient with respect to the membrane proteins, it avoids the danger of ligands being compressed during contact between the tip and the cell surface, and it allows a clear distinction between specific and unspecific binding because of the soft and nonlinear elasticity of the PEG linker [34, 36]. Furthermore, because the PEG is covalently bound to both the tip and the ligand, its binding strength is much stronger than the protein–ligand bond. Thus, the membrane protein–ligand bond ruptures first during retraction and therefore ensures that the measured force is associated only with the protein–ligand binding. To perform single-molecule measurements, the density of ligands linked to the tip must be low enough (fluorescence labeling can be used to estimate the number of ligands in the contact area of a tip of known radius [40]) to ensure that only one protein–ligand bond forms [41].

In order to link rituximab to the surface of AFM tip, NHS–PEG–MAL linker (JenKem Technology, Beijing, China) was used here. Commercial rituximab stock solution (10 mg ml^{-1}) was obtained from Chinese Affiliated Hospital of Military Medical Academy of Sciences. The silicon nitride probe (Bruker, Santa Barbara, CA, USA) was used for functionalization. The process of tip functionalization was according to the Ref. [42, 43]. Aminopropyltriethoxysilan (APTES) (30 µl) and *N*,*N*-diisopropylethylamine (10 µl) were used to coat the AFM stylus with the NH_2 groups under argon gas in a glass desiccator for 0.5–2 h. The PEG linker and triethylamine were mixed in chloroform and then incubated with the NH_2-modified probes for 2–3 h, which allowed the NHS end of the PEG linker to covalently bind to the NH_2 groups on the surface of AFM tip. Rituximab was treated with SATP to form thiol functional groups. Finally, the probes were placed in the SATP–rituximab mixture containing hydroxylamine and buffer solution (pH 7.5) for 1 h, which allowed the MAL end of the PEG linker to bind to the thiols on the rituximab. The functionalized probes were stored in phosphate buffered saline (PBS) at 4 °C. In order to demonstrate the activity of the rituximab-functionalized probe, force curves were obtained on the surface of lymphoma Raji cells, as shown in Figure 17.3a. Raji cell is a Burkitt's lymphoma cell line and expresses CD20 on the cell surface. We can see that there was an unbinding peak in the retract curve, as denoted by the arrow in Figure 17.3a. The unbinding peak was determined by the change in the slope during the retract process, which reflected the stretching of the flexible linker molecules [44]. A key feature in molecular recognition studies by SMFS is to demonstrate the specificity of the measured unbinding forces, which can be achieved by block experiments [33]. Here, force curves were obtained on Raji cells again after adding free rituximabs, and a typical force curve is shown in Figure 17.3b. We can see that the unbinding peak vanished, which demonstrated that the unbinding peak in Figure 17.3a corresponded to the CD20–rituximab interactions. The experimental results in Figure 17.3 indicated the activity of the rituximab-functionalized probe.

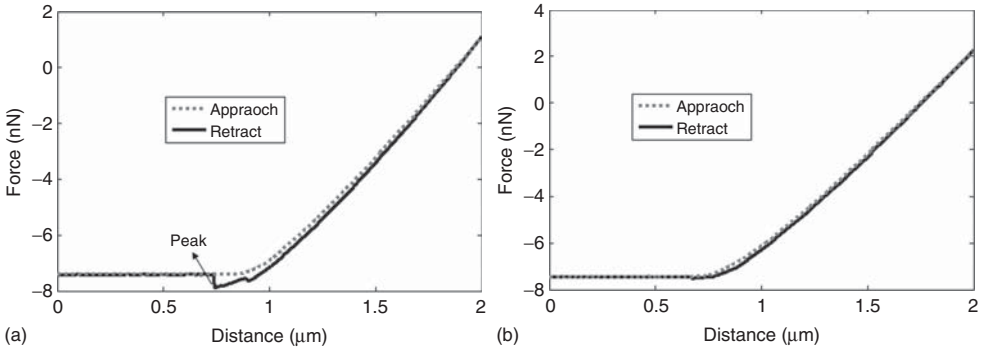

Figure 17.3 The use of rituximab-conjugated probe to obtain force curves on lymphoma Raji cells. (a) A typical force curve (with unbinding peak) obtained on Raji cells. (b) A typical force curve obtained on rituximab-blocked Raji cells. (Reprinted with permission from Ref. [43]. Copyright 2011 Science China Press.)

17.3
Force Spectroscopy of Molecular Interactions on Tumor Cells from Patients

B cells are a type of lymphocyte that expresses clonally diverse cell surface immunoglobulin (Ig) receptors recognizing specific antigenic epitopes [45]. B cells can produce antibodies, which make them perform as positive regulators of immune responses and central contributors to the pathogenesis of immune-related diseases [46]. B-cell NHL results from the process of canceration by which healthy B cells transformed into cancer B cells. B-cell NHL commonly involves the bone marrow invasion. The bone marrow samples (obtained from B-cell NHL patients with bone marrow invasion) contain cancer B cells, healthy B cells, and other healthy cells. Both cancer B cells and healthy B cells express CD20. Rituximab can bind to CD20s on the surface of both cancer B cells and healthy B cells, and this binding then leads to the cell lysis via several mechanisms [23]. We are interested in the binding of rituximab to the CD20s on the surface of cancer B cells, because this binding has direct impact on the rituximab's treatment efficacies. In order to investigate the CD20 on cancer B cells, we need to recognize cancer B cells first. Recent research work indicate that receptor tyrosine kinase-like orphan receptor 1 (ROR1) is a specific cell surface marker expressed on some B-cell lymphomas (such as mantle cell lymphoma, marginal zone lymphoma, diffuse B-cell lymphoma, and follicular lymphoma) but not on virtually all normal adult tissues [47, 48]. Hence, ROR1 is a suitable marker for distinguishing tumor B cells from healthy cells.

We first tested the ROR1 fluorescence labeling on Raji cells. Figure 17.4a–d shows the ROR1 fluorescence labeling experimental results of Raji cells. Raji cells were cultured in RPMI-1640 medium containing 10% fetal bovine serum at 37 °C (5% CO_2) for 24 h before experiments. Cells were harvested at 1000 rpm for 5 min. After removing the supernatant, the cells were resuspended by PBS. Then, a drop of cell suspension was placed on a poly-L-lysine-coated glass slide

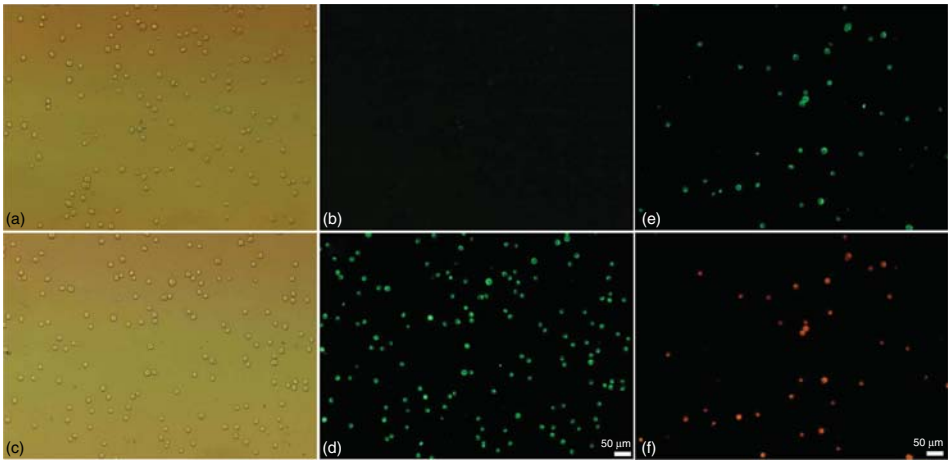

Figure 17.4 ROR1 fluorescence labeling of Raji cells. (a) Optical image of the control group. (b) Fluorescence image of the control group. (c) Optical image of the ROR1 group. (d) Fluorescence image of the ROR1 group. (e,f) ROR1 and CD20 labeling of Raji cells. (e) ROR1 fluorescence image of Raji cells. (f) CD20 fluorescence image of Raji cells. (Reprinted with permission from Ref. [49]. Copyright 2013 John Wiley & Sons, Ltd.)

and subsequently fixed for 30 min with 4% paraformaldehyde. The procedure of fluorescence labeling experiments was the following: (i) After washing the prepared sample three times (each time 10 min) with PBS, add donkey blocking serum and then incubate for 30 min at room temperature. (ii) Add 40 μl goat-antihuman-ROR1 antibody solution (R&D company, USA), incubate for 3 h at room temperature. For control experiment, ROR1 antibody was not added. (iii) Wash the sample three times with PBS, and then add 20 μl FITC-conjugated donkey-antigoat IgG (Kangchen company, Shanghai, China), and incubate for 30 min. (iv) Wash the sample three times with PBS, and place it onto the stage of the fluorescence microscope (Ti, Nikon company, Japan). Goat-antihuman-ROR1 antibody can bind to the ROR1 on the cell surface and FITC-conjugated donkey-antigoat IgG can bind to the goat-antihuman ROR1 antibody. If there was ROR1 on the cell surface, then the cell displayed green light after the excitation of blue light. Figure 17.4a was the optical image of control group and Figure 17.4b was the corresponding fluorescence image. Figure 17.4c was the optical image of ROR1 group and Figure 17.4d was the corresponding fluorescence image. We can see that Raji cells did not exhibit fluorescence without ROR1 antibody (Figure 17.4b). While cells exhibit bright green fluorescence with ROR1 antibody (Figure 17.4d), these experiments indicate that Raji cells express ROR1. ROR1 is the receptor tyrosine kinase-like orphan receptor 1 and functional data suggest that ROR1 may act in Wnt-signaling and promote the survival of malignant cells [49, 50]. Raji cell line is from a Burkitt's lymphoma patient, which is a subtype of B-cell NHL. Previous research works have shown that several B-cell lymphomas express ROR1 [47] and here we can see that Burkitt's lymphoma also express

ROR1. Our goal is to measure the CD20–rituximab binding force based on the ROR1 fluorescence recognition, and in order to examine whether the ROR1 fluorescence labeling influence the CD20s on the cell surface, we perform CD20 fluorescence labeling experiments on ROR1-labeled cells (Figure 17.4e,f). The color of fluorescent dye of ROR1 labeling experiments was green (FITC) and in order to discriminate the color, we chose a red fluorescent dye (RBITC) for CD20 labeling experiments. Figure 17.4e was the ROR1 fluorescence image and Figure 17.4f was the corresponding CD20 fluorescence image. The optical image was not shown. We can see that after ROR1 labeling, the cells still exhibit red fluorescence indicating that there are CD20s on the cell surface.

The results of Figure 17.4 indicated that there were CD20s on the ROR1-labeled cells and we then examined whether the CD20–rituximab binding force can be measured on ROR1-labeled cells. Rituximab was linked onto the AFM tip surface and SMFS technique was applied to measure the CD20–rituximab binding force on the cell surface. Raji cells were chemically fixed by 4% paraformaldehyde. The experiments were performed in PBS. Dimension 3100 AFM (Veeco, Santa Barbara, CA, USA) was used. First, the AFM tip was moved onto the surface of Raji cells under the guidance of optical microscopy and the cell morphology was acquired by AFM imaging at contact mode. Figure 17.5a was the AFM height image and Figure 17.5b was the AFM deflection image of a Raji cell. Then the AFM tip was localized to the small area of the cell surface and force curves were obtained by converting the imaging mode into force measurement mode. Figure 17.5c was a typical force curve obtained on the ROR1-labeled Raji cells. Each force curve contains two curves, approach curve and retract curve. The approach curve corresponded to the approach process during which the tip carrying rituximab approached and touched the cells. When the tip did not touch the cell surface, the curve was flat. After touching the cell surface, the curve bent. The retract curve corresponded to the retract process during which the tip moved back from the cell surface. The rituximab density on the tip surface was controlled to be low to ensure that only one CD20–rituximab complex formed

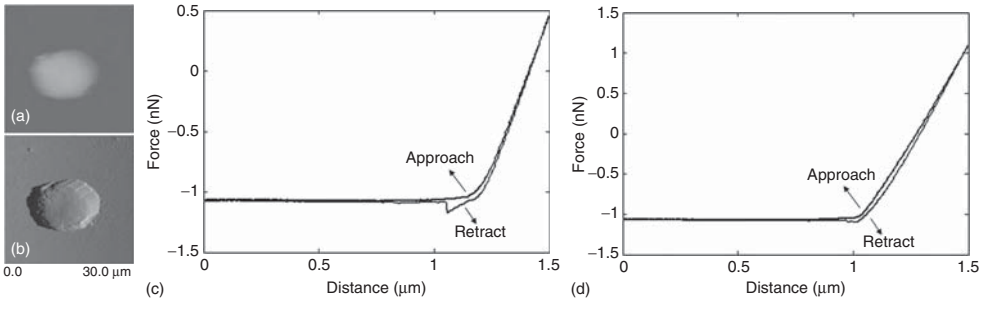

Figure 17.5 Obtaining force curves on ROR1-labeled Raji cells. (a) AFM height image and (b) deflection image of a Raji cell. (c) A typical force curve with CD20–rituximab-specific binding occurred. (d) A typical force curve after blocking. (Reprinted with permission from Ref. [49]. Copyright 2013 John Wiley & Sons, Ltd.)

during each approach–retract cycle. If CD20–rituximab complex formed during the approach–retract cycle, then there would be a specific peak in the retract curve, which indicated the rupture of CD20–rituximab complex. We can see that there was a peak in the retract curve. The shape of the peak indicated that specific molecular binding occurred during the approach–retract process. In order to validate that the binding was from CD20–rituximab, we added free rituximab into the solution to block the CD20s on the cell surface and then obtained force curves again. A typical force curve after blocking was shown in Figure 17.5d. We can see that there was only a tiny peak in the retract curve and the peak shape indicated that it was nonspecific binding. This demonstrated that the unbinding peak in the retract curve corresponded to the CD20–rituximab interactions on the surface of Raji cells.

The above results indicated that CD20–rituximab binding force can be measured on ROR1-labeled Raji cells. Then, we applied the established procedures on pathological cells prepared from the bone marrow of a follicular lymphoma patient whose bone marrow had been invaded by cancer cells. Because fluorescence was required to recognize the cancer cells, BioScope Catalyst AFM (Bruker, Santa Barbara, CA, USA) was used. Follicular lymphoma is a subtype of B-cell NHL, and previous research works have indicated that follicular lymphoma cells express ROR1 [47]. The pathological cell samples contained normal cells and cancer cells. Since only cancer cells express ROR1 (normal cells do not express ROR1), they can be recognized by ROR1 fluorescence labeling. Figure 17.6 shows the AFM imaging of cancer cells assisted by the ROR1 fluorescence recognition. Figure 17.6a was the optical image, Figure 17.6b was the fluorescence image, and Figure 17.6c was the merge of optical and fluorescence images. From the fluorescence image (Figure 17.6b), there was a clear cancer cell that exhibited bright fluorescence (denoted by the white circle). From the inset of the merge image (Figure 17.6c), we can see many normal cells around the shining cancer cell. Under the guidance of fluorescence, the AFM probe was moved onto the cancer cell to image the cellular morphology. The imaging mode was contact mode and both height image and deflection error image were obtained. Figure 17.6d was the height image and Figure 17.6e was the deflection error image. The range of AFM image (50 μm) corresponded to the area denoted by the red dotted square in Figure 17.6c. The color range of the height image was 15 μm and the color range of the deflection error image was 1.5 μm. The cancer cell can be clearly discerned in AFM images (denoted by the square in Figure 17.6d). The section curve (Figure 17.6f) indicated that the height of the cell was about 3 μm and the diameter was about 13 μm. Most current AFM imaging experiments were performed on cells cultured *in vitro* [51]. Here we imaged the cellular morphology of cancer cells from patients under the assistance of fluorescence recognition. We know that cells grown *in vitro* can be quite different from those grown *in vivo*, thus directly investigating the behavior of primary cells from clinical patients is of great significance for us to understand the underlying mechanisms that regulate the cellular activities. However, it should be noted that the patient cancer cells here for AFM imaging were chemically fixed and thus lost

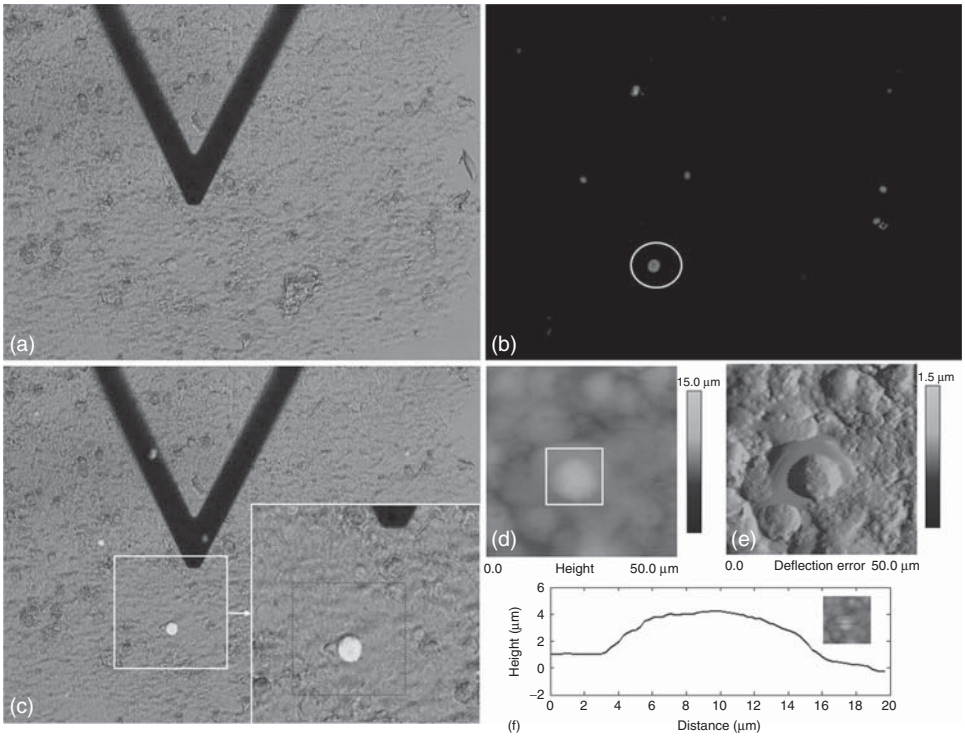

Figure 17.6 Under the guidance of ROR1 fluorescence, AFM probe was moved to the cancer cell to image the cellular morphology. (a) Optical image and (b) fluorescence image of the pathological cell sample. (c) Merge image of optical and fluorescence images. (d) AFM height image of the cancer cell (denoted by the red square in (c)). (e) AFM deflection error image of the cancer cell. (f) Section curve. (Reprinted with permission from Ref. [49]. Copyright 2013 John Wiley & Sons, Ltd.) (For color version, the reader is referred to the Web version of the Ref. [49].)

living activity. In the future, we want to obtain the topography images of living cancer cells from clinical patients. In this situation, we should isolate and collect tumor cells, for example, by flow cytometry [52]. Besides, due to the suspended trait of the lymphoma cell, we should develop adequate methods to immobilize them for living-cell AFM imaging, for example, micro well array chip [53] and thin film having small pores [54]. Investigating the behavior of living tumor cells from patients will enable us to detect and monitor the physiological properties of living tumor cells (e.g., the cellular changes after the stimulation of drugs), bringing novel information that is closer to the real cellular activities.

Then the AFM imaging mode was converted into force measurement mode and force curves were obtained on the ROR1-labeled cancer cells. Figure 17.7a was a typical force curve obtained on the cancer cell. We can see that in the retract curve there was a specific peak which indicated the CD20–rituximab binding. Because there is a change in the slope during the retraction process which is a result of a

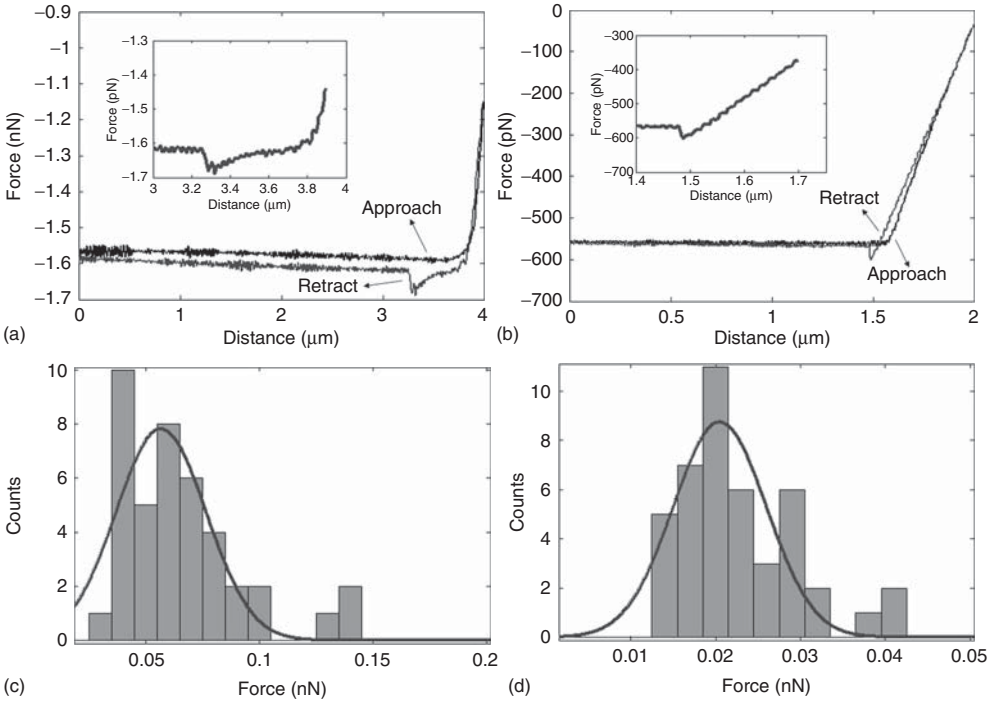

Figure 17.7 Measuring the CD20–rituximab binding force on patient cancer cells. (a) A typical force curve obtained on cancer cells. The inset was the amplifying plot of the retract curve. (b) A typical force curve obtained on normal cells. The inset was the amplifying plot of the retract curve. (c) Histogram of CD20–rituximab binding forces on cancer cells. (d) Histogram of non-specific binding forces on normal cells. (Reprinted with permission from Ref. [49]. Copyright 2013 John Wiley & Sons, Ltd.)

decreased effective spring constant [44], the specific peak can be clearly discerned when zooming in the retract curve. Follicular lymphoma patient cancer cells had CD20s on the cell surface and the CD20–rituximab complex formed during the approach–retract cycle with rituximab-conjugated tip. Also, force curves on normal cells, which did not exhibit fluorescence, were obtained and a typical force curve was shown in Figure 17.7b. We can see that the force curve on normal cells had only a tiny non specific peak in the retract curve where there is not a change in the slope. The non specific peak indicated the non specific molecular binding. Healthy cells in the pathological sample prepared from patient's bone marrow contain normal B cells and other cells, such as T cells and NK cells. If the force curves were obtained on normal B cells, then there should be specific peak in the force curve, but there was not specific peak in the force curve in Figure 17.7b. Hence, the force curve in Figure 17.7b was not obtained on normal B cells but on other normal cells. From the retraction curve with specific peak obtained on cancer cells, the CD20–rituximab binding force was computed: the binding force was equal to the magnitude of the peak. Because of the random spatial orientation of the binding

partners at the tip and cell surface, it is usually necessary to collect many force curves to determine the distribution of the binding force [44]. The histogram of the CD20–rituximab binding forces was shown in Figure 17.7c. Gaussian fit of the histogram indicated that the binding force was 57 ± 28 pN. The histogram of the non specific binding forces on normal cells was shown in Figure 17.7d and Gaussian fit of the histogram indicated that the non specific binding force was 21 ± 7 pN. We can see that non specific binding force was significantly lower than the specific binding force. The CD20–rituximab binding forces were measured at four different loading rates and the relationship between binding force and loading rate was shown in Figure 17.8. We can see that the binding force is linearly related to the logarithm of the loading rate. This phenomenon can be explained by Bell–Evans model [55], which characterizes the behavior of molecular unbinding pulled by an external force. SMFS is a mature single-molecule technique and many researchers have used SMFS to measure the molecular binding force on cells grown *in vitro*, such as receptor–drug [41], receptor–ligand [56], fibrinogen–erythrocyte [57], and aptamer–protein [58], showing that the binding force of receptor–ligand was in the range of 20–200 pN [59]. Here, we measured the CD20–rituximab binding force on patient cancer cells based on the fluorescence recognition of the specific cancer cell surface marker and the binding force was in the range of molecular binding force. Directly investigating the molecular interactions on cancer cells from clinical patients is of special significance. We know that the prerequisite for personalized medicine is having accurate diagnostic tests that identify patients who can benefit from the therapy [60]. This requires an accurate characterization of the pathology. However, current biochemical research is usually performed on

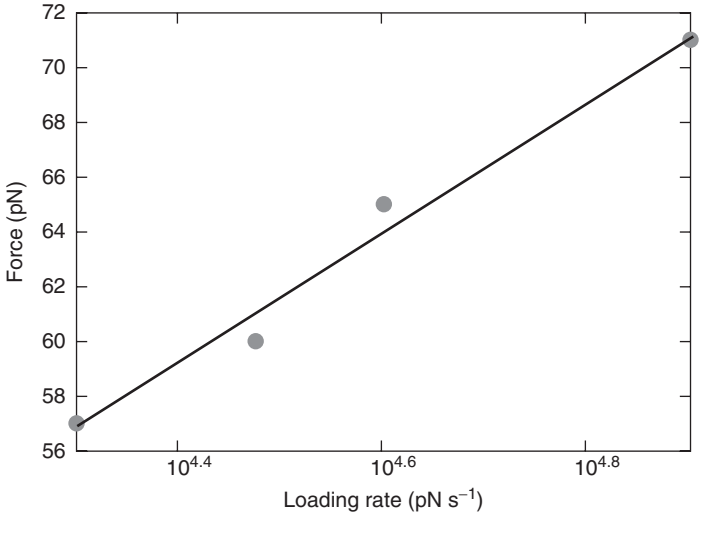

Figure 17.8 The CD20–rituximab binding force is linearly related to the logarithm of loading rates. (Reprinted with permission from Ref. [49]. Copyright 2013 John Wiley & Sons, Ltd.)

cells grown *in vitro*, leaving a large gap between laboratory results and clinical requirements. If we can directly investigate the behavior of tumor cells in the biopsy samples from patients, then we can get more valuable information. Combining such information with clinical data will likely lead to the development of novel, meaningful biomarkers. AFM single-cell and single-molecule techniques were used here to directly investigate the affinity of target proteins (CD20) on tumor cells from clinical patients with the assistance of the specific tumor cell surface biomarker ROR1. This work provided novel insights concerning biophysical properties of target proteins in near *in vivo* conditions, and provided a new way to explore potentially meaningful biomarkers for clinical practice.

17.4 Mapping the Distribution of Membrane Proteins on Tumor Cells

By using SMFS at force volume mode, we can also detect the distribution of membrane proteins on the cell surface [61]. At this mode, AFM tips carrying specific molecules (e.g., antibodies and ligands) were controlled to obtain arrays of force curves at the local areas on the cell surface. To map the distribution of CD20 on the surface of cancer cells, arrays of force curves (16×16) were obtained in the local areas ($500\,\text{nm} \times 500\,\text{nm}$) of the cancer cell. Each force curve corresponds to an adhesion force. After converting these forces into the gray colors (0–255), then a force map was constructed. The map reflects the distribution of CD20 on the cell surface. Figure 17.9 shows the results of mapping the nanoscale distribution of CD20 on the surface of tumor cells. First, under the guidance of ROR1 fluorescence, cancer cells were recognized. Figure 17.9a was the overlay image of bright field image and fluorescence image. We can see one cancer cell in the overlay image, as denoted by the red square. Then, AFM tip carrying rituximabs was moved to the cancer cell to obtain the cellular topography images. Figure 17.9b was the AFM height image of the cancer cell and Figure 17.9c was the corresponding deflection image. Figure 17.9d,e shows AFM images of three healthy cells denoted by the blue square in Figure 17.9a. From the AFM images of the three cells, we can see that cell 1 was a red blood cell due to the special shape of oval biconcave disk. Because red blood cell does not express CD20 on the cell surface, it can be used for negative control experiments.

Then, imaging mode was converted into force curve mode and 16×16 force curves were obtained at the $500\,\text{nm} \times 500\,\text{nm}$ areas on the surface of cancer cells and healthy cells. By analyzing the force curves, adhesion force gray maps were constructed using image processing software. In order to statistically characterize the nanoscale distribution of CD20 on the surface of cancer cells, we obtained force curves on eight cancer cells with five functionalized tips. For each cell, we obtained several distribution maps on different areas on the cell surface. The representative maps were shown in Figure 17.9f. From the force maps of cancer cells, there were many bright pixels, whereas only few gray pixels in the maps of red blood cells and these pixels were dim. From the distribution maps, we can

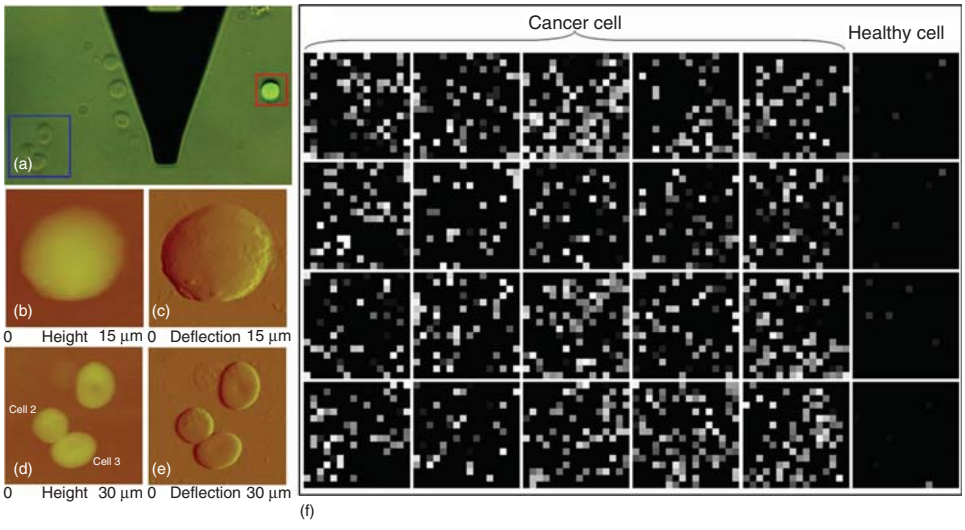

Figure 17.9 Mapping the nanoscale distribution of CD20 on tumor cells. (a) Overlay of optical bright field and fluorescence images. (b) AFM height and (c) deflection image of the tumor cell indicated by the red square in (a). (d) AFM height and (e) deflection image of the three healthy cells indicated by the blue square in (a). (f) CD20 distribution maps on cancer cells and healthy cells. The gray scale bar was 0–100 pN. (Reprinted with permission from Ref. [61]. Copyright 2013 Elsevier Inc.

see that the CD20 distribution on the cell surface was non uniform. The number of CD20 molecules was variable in different local $500 \times 500\,nm^2$ area on the cell surface. In some other areas on the cell surface, there were more CD20 molecules, whereas in some areas, there were less CD20 molecules. We know that cell membranes are heterogeneous in composition, and the structures responsible for this heterogeneity are lipid rafts [62]. Lipid rafts are fluctuating nanoscale assemblies of sphingolipid, cholesterol, and proteins that can be stabilized to coalesce, forming platforms that function in membrane signaling and trafficking [63]. Besides, cell membrane are dynamic (proteins are free to move with the lipid bilayer), and this means that the distribution of membrane proteins on the cell surface changes dynamically. Recently, researchers have directly observed the motion of single-membrane proteins by using high-speed AFM [64]. In addition, cell membranes have variable membrane curvatures in different positions on the cell surface and these curvatures are dynamically remodeled during physiological processes [65]. All these features of cell membranes may cause the results that the distributions of CD20s on the cancer cell surface are non uniform. On the force maps of red blood cells, there were few gray pixels, which were dim. Red blood cells do not express CD20 and hence their maps were dim.

In order to demonstrate that the maps reflect the CD20 distribution on the cell surface, verification experiments were performed, as shown in Figure 17.10. Figure 17.10a shows the merged image of optical and fluorescence images of the clinical bone marrow cell sample and we can see two cancer cells in the image.

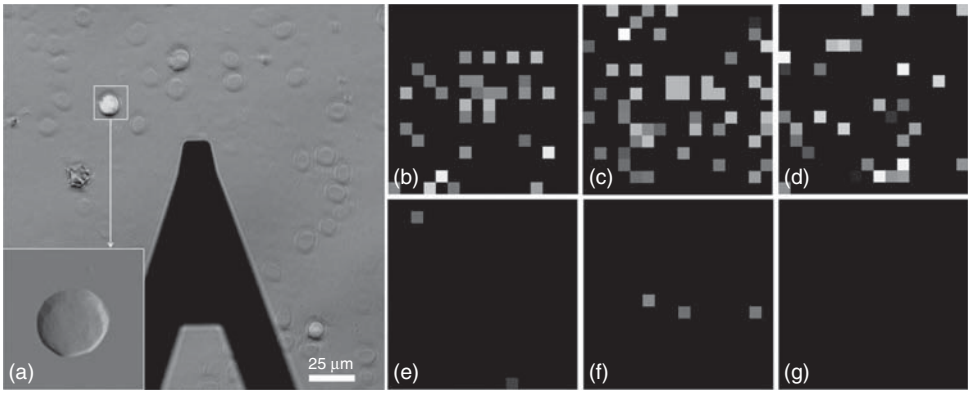

Figure 17.10 Verification of specific CD20–rituximab interactions on cancer cells. (a) Merged image of optical image and fluorescence image of the clinical bone marrow cell sample. The inset is the AFM image of the cancer cell. (b–d) CD20 distribution maps on the cancer cells. (e–g) CD20 distribution maps on the cancer cells after blocking. The gray scale bar was 0–100 pN. (Reprinted with permission from Ref. [61]. Copyright 2013 Elsevier Inc.) (For color version, the reader is referred to the web version of the Ref. [61].)

Under the guidance of fluorescence, AFM-functionalized tips were moved to the cancer cells to image the cell morphology and obtain force curves on the cell surface. From the distribution maps (Figure 17.10b–d), we can see that there are many gray pixels which is consistent with the results in Figure 17.9. After blocking, arrays of force curves were obtained again on the cancer cells, and the distribution maps are shown in Figure 17.10e–g. We can see that after blocking, the gray pixels dramatically decreased, which is because that the CD20s on the cancer cells had been blocked. The results in Figure 17.10 demonstrate the specific CD20–rituximab recognition on the cell surface and therefore the force maps reflect the distribution of CD20s on the cancer cells.

By applying the established method described earlier on the bone marrow cells from three clinical B-cell NHL patients, we obtained the binding affinity and nanoscale distribution of CD20 on the tumor cells for the three patients [66], as shown in Figure 17.11. To investigate the CD20 affinity and nanoscale distribution of different lymphoma patients, we selected three B-cell NHL patients for the study. All of the three patients were with bone marrow infiltration. ROR1 fluorescence labeling experiments were performed to confirm that there were ROR1s on the tumor cell surface of the three patients. The clinical data of the three patients was shown in Table 17.1. For each patient, their bone marrow cells were dropped onto the glass slides and subsequent chemical fixation and ROR1-fluorescence labeling were performed. And then under the guidance of ROR1 fluorescence, about 10 tumor cells were selected and arrays of force curves were obtained on five different local areas on the surface of each cell using functionalized AFM tips. Figure 17.11a–c were the CD20 binding affinities of tumor cells from patient 1, patient 2, and patient 3, respectively. The CD20

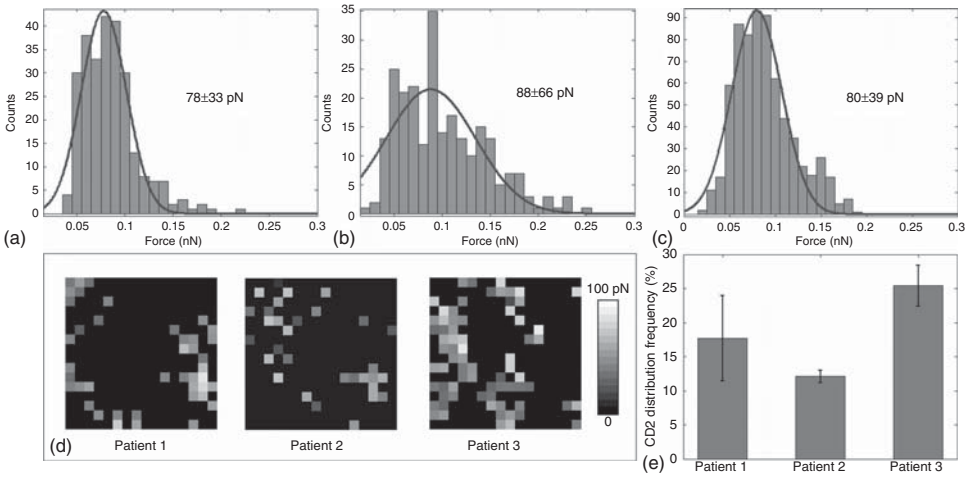

Figure 17.11 Comparison of CD20 binding affinity and nanoscale distribution of tumor cells from three different B-cell NHL patients. The CD20 binding affinity of tumor cells of patient 1 (a), patient 2 (b), and patient 3 (c). (D) Typical adhesion force maps of the three patients. (e) The CD20 distribution frequencies of the three patients. (Reprinted with permission from Ref. [66]. Copyright 2014 Royal Microscopical Society.)

Table 17.1 Clinical information of three clinical lymphoma patients.

Case no.	Sex	Age	Tumor subtype	Clinical therapy	Therapy outcome
1	Female	64	Splenic marginal zone B-cell lymphoma	Rituximab + Fludarabine + Cyclophosphamide	Complete remission
2	Male	56	Small B-cell lymphoma	Rituximab + CHOP	Lesion stability
3	Female	51	Diffuse large B-cell lymphoma	Rituximab + CHOP	Partial remission

Reprinted with permission from Ref. [66]. Copyright 2014 Royal Microscopical Society.

binding affinities to rituximab were computed from the force curves which had specific molecular unbinding peaks. From the histogram, the Gaussian fitting indicated that the CD20 binding affinities of the three patients were 78 ± 33, 88 ± 66, 80 ± 39 pN, respectively. We can see that the binding affinities were not a remarkable variable between the three patients. Figure 17.11d shows the typical adhesion force maps of the three patients. To quantitatively characterize the nanoscale distribution of CD20s, we calculate the CD20 distribution frequency for each adhesion force map to characterize the CD20 density of the cells. For each adhesion force map, we can compute the number of gray and bright pixels (n), and the number of overall pixels of the adhesion force map was known ($16 \times 16 = 256$). The CD20 distribution frequency of this adhesion force map was equal to the

ratio (n/256). Figure 17.11e shows the CD20 distribution frequencies of the three patients. Analyzing the relationship between CD20 density and clinical therapy outcomes, we can find some interesting phenomenon. The combined therapy (rituximab + chemotherapy) was effective for patient 1 and patient 3, but was ineffective for patient 2, while the histogram of distribution frequencies indicated that the CD20 density of patient 2 was the smallest. This indicated that if there were more CD20s on the surface of tumor cells, the clinical efficacy was better. However, the efficacy of patient 3 was worse than that of patient 1, while the CD20 density of patient 3 was larger than that of patient 1. This indicated that the therapy effects were not linearly proportional to the CD20 density of the tumor cells. The experimental results showed that the clinical efficacy of rituximab was to some extent related to the CD20 density, and the relationship was not linear but may be complicated.

We know that the main theory in pharmacology to characterize the efficacies of drugs is receptor theory [67]. Drugs produce therapeutic effects by binding to the receptors on the cell surface. Hence it is reasonable that when more drug molecules bind to the receptors on the cell surface, the effects become stronger. But the drug effects are not linearly proportional to the number of receptors occupied and the maximum effect can be produced by a drug when occupying just only a small proportion of the receptors [68]. The experimental results here indicated that the variance of CD20 binding affinities was not prominent among the three lymphoma patients in the study here, while the CD20 density of tumor cells was related to the efficacy of the clinical treatment. When rituximabs bind to the CD20s on the tumor cell, the Fc domains of rituximab can bind to the FcRs on the effector cells, which can then kill the tumor cells. The Fc domains of rituximab can also activate the classical complement pathway, which eventually causes the lysis of the tumor cells [17]. Compared to the binding affinity between CD20 and rituximab, the CD20 density on the cell surface may play a more important role in the rituximab's therapy effects. If there are more CD20s on the tumor cell surface, then possibly more rituximabs can bind to the cell surface and more effector cells can be recruited, which causes that the therapy effects become stronger. But there may exist a threshold of the number of CD20 on the surface of tumor cells. If the number of CD20s exceeds this threshold, the efficacies of rituximab do not increase, as the observed phenomenon of patient 1 and patient 3. Researchers [69] have investigated the relationship between CD20 expression level and rituximab-mediated cell kill and the results indicated that rituximab-induced CDC clearly depends on the CD20 expression level. While in the rituximab's killing mechanisms, rituximab displays a remarkable ability to activate complement and elicit CDC [16]. These evidence indicated that CD20 expression is closely related to the therapeutic effects of rituximab. However, exactly elucidating the mechanisms that determine the clinical efficacies of rituximab is a challenge. First, even though the rituximab's three mechanisms have been demonstrated *in vitro*, the situations *in vivo* is not unknown. Limited by the technique, we now cannot investigate the drug actions in the human body, meaning that we can only obtain conclusions by indirect methods (e.g., *in vitro* test and

animal model), which cannot reflect the real behavior in the human [70]. Second, the rituximab is typically combined with chemotherapy in the practice, and thus the contribution of rituximab to the efficacy is difficult to evaluate [71]. Third, the problem of rituximab's variable efficacies among different patients is complicated, and various aspects need to be taken into consideration, such as tumor profiling, analysis of the microenvironment, assessment of host immune effector function, and genetic polymorphisms of FcR [23]. Here, we investigated the relationship between CD20 density of tumor cells and the clinical therapy effects, and the results indicated that the therapy effects are related to the CD20 density in a certain range. However, we only investigated three clinical lymphoma cases, and more cases are needed to be investigated in the future to obtain a robust result.

In the future, we want to collect more lymphoma cases to investigate the biophysical properties of tumor cells. Besides the binding affinity and distribution of CD20 on the tumor cells, we would like to measure the binding affinity and distribution of FcRs on the effector cells (e.g., NK cell and macrophage) from the patients. We know that the efficacies of rituximab are related not only to the tumor but also to the host immune systems. In the ADCC action of rituximab, rituximab binds to the CD20 on the tumor cells, and then the Fc domain of rituximab binds to the FcR on the effectors. We can see that two types of molecular interactions occur in ADCC, including CD20–rituximab and FcR–rituximab. Many experiments have demonstrated that FcR plays a central role in the killing mechanism of rituximab [17], and several new anti-CD20 antibodies (e.g., Ofatumumab, Ocrelizumab, Veltuzumab, AME-133V, PRO131921, GA101) with enhanced FcR-mediated effector functions have been developed for clinical trials [23]. Clinical trials of these new antibodies will help us to know which mechanism of rituximab is indispensable in the therapy [26]. Consequently, simultaneously measuring the molecular interactions of CD20–rituximab and FcR–rituximab will significantly improve our understanding of rituximab action and may bring meaningful information.

17.5 Summary

Developing personalized drugs for the subpopulations of patients has become the trend of treating major diseases such as cancer, which will bring far-reaching impact on biomedical and pharmaceutical industry. The success of personalized medicine depends on having accurate diagnostic tests that indent patients who can benefit from targeted therapies [60]. However, current biochemical techniques have several serious deficiencies, such as low resolution, difficult to quantify, offline testing, and cannot reveal the heterogeneity between cells. The invention of AFM provides a powerful tool for investigating the cellular behavior at single-cell and single-molecule levels. The wide use of AFM-based SMFS technique has provided a wealth of novel knowledge about the physiological activities of single molecules on the cell surface, improving our understanding of

the underlying mechanisms that guide cellular functions. AFM has been proven to be an exciting tool for analyzing the heterogeneity between cells and will play an important role in the era of personalized medicine.

Acknowledgments

This work was partly supported by the National Natural Science Foundation of China (Project No. 61175103, 61327014) and CAS FEA International Partnership Program for Creative Research Teams.

References

1. Jemal, A., Bray, F., Center, M.M., Ferlay, J., Ward, E., and Forman, D. (2011) Global cancer statistics. *CA Cancer J. Clin.*, **61**, 69–90.
2. Bray, F., Jemal, A., Grey, N., Frelay, J., and Forman, D. (2012) Global cancer transitions according to the human development index (2008-2030): a population-based study. *Lancet Oncol.*, **13**, 790–801.
3. Schwarzenbach, H., Hoon, D.S.B., and Pantel, K. (2011) Cell-free nucleic acids as biomarkers in cancer patients. *Nat. Rev. Cancer*, **11**, 426–437.
4. Patel, J.D. *et al* (2014) Clinical cancer advances 2013: annual report on progress against cancer from the American society of clinical oncology. *J. Clin. Oncol.*, **32**, 129–160.
5. Varmus, H. (2006) The new era in cancer research. *Science*, **312**, 1162–1165.
6. Shankland, K.R., Armitage, J.O., and Hancock, B.W. (2012) Non-hodgkin lymphoma. *Lancet*, **380**, 848–857.
7. Siegel, R., Naishadham, D., and Jemal, A. (2013) Cancer statistics, 2013. *CA Cancer J. Clin.*, **63**, 11–30.
8. Campo, E., Swerdlow, S.H., Harris, N.L., Pileri, S., Stein, H., and Jaffe, E.S. (2011) The 2008 WHO classification of lymphoid neoplasms and beyond: evolving concepts and practical applications. *Blood*, **117**, 5019–5032.
9. Cheson, B.D. and Leonard, J.P. (2008) Monoclonal antibody therapy for B-cell non-Hodgkin's lymphoma. *N. Engl. J. Med.*, **359**, 613–626.
10. Kuppers, R. (2005) Mechanisms of B-cell lymphoma pathogenesis. *Nat. Rev. Cancer*, **5**, 251–262.
11. Morin, R.D. *et al* (2011) Frequent mutation of histone-modifying genes in non-Hodgkin lymphoma. *Nature*, **476**, 298–303.
12. Deans, J.P., Li, H., and Polyak, M.J. (2002) CD20-mediated apoptosis: signaling through lipid rafts. *Immunology*, **107**, 176–182.
13. Boross, P. and Leusen, J.H.W. (2012) Mechanisms of action of CD20 antibodies. *Am. J. Cancer Res.*, **2**, 676–690.
14. Cragg, M.S., Walshe, C.A., Ivanov, A.O., and Glennie, M.J. (2005) The biology of CD20 and its potential as a target for mAb therapy. *Curr. Dir. Autoimmun.*, **8**, 140–174.
15. Perosa, F., Prete, M., Racanelli, V., and Dammacco, F. (2010) CD20-depleting therapy in autoimmune diseases: from basic research to the clinic. *J. Int. Med.*, **267**, 260–277.
16. Beers, S.A., Chan, C.H.T., French, R.R., Cragg, M.S., and Glennie, M.J. (2010) CD20 as a target for therapeutic type I and II monoclonal antibodies. *Semin. Hematol.*, **47**, 107–114.
17. Glennie, M.J., French, R.R., Cragg, M.S., and Taylor, R.P. (2007) Mechanisms of killing by anti-CD20 monoclonal antibodies. *Mol. Immunol.*, **44**, 3823–3837.
18. Leandro, M.J. (2013) B-cell subpopulations in humans and their differential susceptibility to depletion with anti-CD20 monoclonal antibodies. *Arthritis Res. Ther.*, **15**, S3.

19. Cartron, G., Watier, H., Golay, J., and Solal-Celigny, P. (2004) From the bench to the bedside: ways to improve rituximab efficacy. *Blood*, **104**, 2635–2642.
20. Lim, S.H., Beers, S.A., French, R.R., Johnson, P.W.M., Glennie, M.J., and Cragg, M.S. (2010) Anti-CD20 monoclonal antibodies: historical and future perspectives. *Haematologica*, **95**, 135–143.
21. Adams, G.P. and Weiner, L.M. (2005) Monoclonal antibody therapy of cancer. *Nat. Biotechnol.*, **23**, 1147–1157.
22. Molina, A. (2008) A decade of rituximab: improving survival outcomes in non-Hodgkin's lymphoma. *Ann. Rev. Med.*, **59**, 237–250.
23. Alduaij, W. and Illidge, T.M. (2011) The future of anti-CD20 monoclonal antibodies: are we making progress. *Blood*, **117**, 2993–3001.
24. Zwick, C., Murawski, N., and Pfreundschuh, M. (2010) Rituximab in high-grade lymphoma. *Semin. Hematol.*, **47**, 148–155.
25. Maloney, D.G. (2012) Anti-CD20 antibody therapy for B-cell lymphomas. *N. Engl. J. Med.*, **366**, 2008–2016.
26. Weiner, G.J. (2010) Rituximab: mechanism of action. *Semin. Hematol.*, **47**, 115–123.
27. Dupres, V., Alsteens, D., Andre, G., Verbelen, C., and Dufrene, Y.F. (2009) Fishing single molecules on live cells. *Nano Today*, **4**, 262–268.
28. Yamada, K.M. and Cukierman, E. (2007) Modeling tissue morphogenesis and cancer in 3D. *Cell*, **130**, 601–610.
29. Binning, G., Quate, C.F., and Gerber, C. (1986) Atomic force microscope. *Phys. Rev. Lett.*, **56**, 930–933.
30. Yu, X., Xu, D., and Cheng, Q. (2006) Label-free detection methods for protein microarrays. *Proteomics*, **6**, 5493–5503.
31. Dufrene, Y.F., Martinez-Martin, D., Medalsy, I., Alsteens, D., and Muller, D.J. (2013) Multiparametric imaging of biological systems by force-distance curve-based AFM. *Nat. Methods*, **10**, 847–854.
32. Li, M., Liu, L., Xi, N., and Wang, Y. (2014) Progress in measuring biophysical properties of membrane proteins with AFM single-molecule force spectroscopy. *Chin. Sci. Bull.*, **59**, 2717–2725.
33. Hinterdorfer, P. and Dufrene, Y.F. (2006) Detection and localization of single molecular recognition events using atomic force microscopy. *Nat. Methods*, **3**, 347–355.
34. Barattin, R. and Voyer, N. (2008) Chemical modifications of AFM tips for the study of molecular recognition events. *Chem. Commun.*, 1513–1532.
35. Dupres, V., Menozzi, F.D., Locht, C. *et al* (2005) Nanoscale mapping and functional analysis of individual adhesions on living bacteria. *Nat. Methods*, **2**, 515–520.
36. Carvalho, F.A. and Santos, N.C. (2012) Atomic force microscopy-based force spectroscopy- biological and biomedical applications. *IUBMB Life*, **64**, 465–472.
37. Grandbois, M., Beyer, M., Rief, M., Clausen-Schaumann, H., and Gaub, H.E. (1999) How strong is a covalent bond. *Science*, **283**, 1727–1730.
38. Merkel, R., Nassoy, P., Leung, A., Ritchie, K., and Evans, E. (1999) Energy landscapes of receptor-ligand bonds explored with dynamic force spectroscopy. *Nature*, **397**, 50–53.
39. Ebner, A., Wildling, L., Kamruzzahan, A.S.M., Rankl, C., Wruss, J., Hahn, C.D., Holzl, M., Zhu, R., Kienberger, F., Blaas, D., Hinterdorfer, P., and Gruber, H.J. (2007) A new, simple method for linking of antibodies to atomic force microscopy tips. *Bioconjugate Chem.*, **18**, 1176–1184.
40. Hinterdorfer, P., Baumgartner, W., Gruber, H.J., Schilcher, K., and Schindler, H. (1996) Detection and localization of individual antibody-antigen recognition events by atomic force microscopy. *Proc. Natl. Acad. Sci. U.S.A.*, **93**, 3477–3481.
41. Shi, X., Xu, L., Yu, J., and Fang, X. (2009) Study of inhibition effect of Herceptin on interaction between Heregulin and ErbB receptors HER3/HER2 by single-molecule force spectroscopy. *Exp. Cell. Res.*, **315**, 2847–2855.
42. Stroh, C., Wang, H., Bash, R., Ashcroft, B., Nelson, J., Gruber, H., Lohr, D., Lindsay, S.M., and Hinterdorfer, P.

(2004) Single-molecule recognition imaging microscopy. *Proc. Natl. Acad. Sci. U.S.A.*, **101**, 12503–12507.
43. Li, M., Liu, L., Xi, N., Wang, Y., Dong, Z., Li, G., Xiao, X., and Zhang, W. (2011) Detecting CD20-rituximab interaction forces using AFM single-molecule force spectroscopy. *Chin. Sci. Bull.*, **56**, 3829–3835.
44. Lee, C.K., Wang, Y.M., Huang, L.S., and Lin, S. (2007) Atomic force microscopy: determining of unbinding force, off rate and energy barrier for protein-ligand interaction. *Micron*, **38**, 446–461.
45. Lebien, T.W. and Tedder, T.F. (2008) B lymphocyte: how they develop and function. *Blood*, **112**, 1570–1579.
46. Mauri, C. and Bosma, A. (2012) Immune regulatory function of B cells. *Ann. Rev. Immunol.*, **30**, 221–241.
47. Barna, G., Mihalik, R., Timar, B., Tombol, J., Csende, Z., Sebestyen, A., Bodor, C., Csernus, B., Reiniger, L., Petak, I., and Matolcsy, A. (2011) ROR1 expression is not a unique marker of CLL. *Hematol. Oncol.*, **29**, 17–21.
48. Zhang, S., Chen, L., Wang-Rodriguez, J., Zhang, L., Cui, B., Frankel, W., Wu, R., and Kipps, T.J. (2012) The onco-embryonic antigen ROR1 is expressed by a variety of human cancers. *Am. J. Pathol.*, **181**, 1903–1910.
49. Li, M., Xiao, X., Liu, L., Xi, N., Wang, Y., Dong, Z., and Zhang, W. (2013) Atomic force microscopy study of the antigen-antibody binding force on patient cancer cells based on ROR1 fluorescence recognition. *J. Mol. Recognit.*, **26**, 432–438.
50. Hudecek, M., Schmitt, T.M., Baskar, S., Lupo-Stanghellini, M.T., Nishida, T., Yamamoto, T.N., Bleakley, M., Turtle, C.J., Chang, W.C., Greisman, H.A., Wood, B., Maloney, D.G., Jensen, M.C., Rader, C., and Riddell, S.R. (2010) The B-cell tumor-associated antigen ROR1 can be targeted with T cells modified to express a ROR1-specific chimeric antigen receptor. *Blood*, **116**, 4532–4541.
51. Casuso, I., Rico, F., and Scheuring, S. (2011) Biological AFM: where we come from – where we are – where we may go. *J. Mol. Recognit.*, **24**, 406–413.
52. Suzuki, A., Sekiya, S., Onishi, M., Oshima, N., Kiyonari, H., Nakauchi, H., and Taniquchi, H. (2008) Flow cytometric isolation and clonal identification of self-renewing bipotent hepatic progenitor cells in adult mouse liver. *Hepatology*, **48**, 1964–1978.
53. Li, M., Liu, L.Q., Xi, N., Wang, Y., Dong, Z., Xiao, X., and Zhang, W. (2013) Atomic force microscopy imaging of live mammalian cells. *Sci. China Life Sci.*, **56**, 811–817.
54. Ando, T. (2012) High-speed atomic force microscopy coming of age. *Nanotechnology*, **23**, 062001.
55. Zhang, J., Wu, G., Song, C., Li, Y., Qiao, H., Zhu, P., Hinterdorfer, P., Zhang, B., and Tang, J. (2012) Single molecular recognition force spectroscopy study of a luteinizing hormone-releasing hormone analogue as a carcinoma target drug. *J. Phys. Chem. B*, **116**, 13331–13337.
56. Puntheeranurak, T., Wildling, L., Gruber, H.J., Kinne, R.K.H., and Hinterdorfer, P. (2006) Ligands on the string: single-molecule AFM studies on the interaction of antibodies and substrates with the Na+-glucose co-transporter SGLT1 in living cells. *J. Cell Sci.*, **119**, 2960–2967.
57. Carvalho, F.A., Connell, S., Miltenberger-Miltenyi, G., Pereira, S.V., Tavares, A., Ariens, R.A.S., and Santos, N.C. (2010) Atomic force microscopy-based molecular recognition of a fibrinogen receptor on human erythrocytes. *ACS Nano*, **4**, 4609–4620.
58. Li, Y., Qiao, H., Yan, W., Zhang, J., Xing, C., Wang, H., Zhang, B., and Tang, J. (2013) Molecular recognition force spectroscopy study of the dynamic interaction between aptamer GBI-10 and extracellular matrix protein tenascin-C on human glioblastoma cell. *J. Mol. Recognit.*, **26**, 46–50.
59. Muller, D.J., Helenius, J., Alsteens, D., and Dufrene, Y.F. (2009) Force probing surfaces of living cells to molecular resolution. *Nat. Chem. Biol.*, **5**, 383–390.
60. Humburg, M.A. and Collins, F.S. (2010) The path to personalized medicine. *N. Engl. J. Med.*, **363**, 301–304.
61. Li, M., Xiao, X., Liu, L., Xi, N., Wang, Y., Dong, Z., and Zhang, W. (2013) Nanoscale mapping and organization analysis of target proteins on cancer cells

from B-cell lymphoma patients. *Exp. Cell. Res.*, **319**, 2812–2821.

62. Sanchez, S.A., Tricerri, M.A., and Gratton, E. (2012) Laurdan generalized polarization fluctuations measures membrane packing micro-heterogeneity in vivo. *Proc. Natl. Acad. Sci. U.S.A.*, **109**, 7314–7319.
63. Lingwood, D. and Simons, K. (2010) Lipid rafts as a membrane-organizing principle. *Science*, **327**, 46–50.
64. Casuso, I., Khao, J., Chami, M., Paul-Gilloteaux, P., Husain, M., Duneau, J.P., Stahlberg, H., Sturgis, J.N., and Scheuring, S. (2012) Characterization of the motion of membrane proteins using high-speed atomic force microscopy. *Nat. Nanotechnol.*, **7**, 525–529.
65. McMahon, H.T. and Gallop, J.L. (2005) Membrane curvature and mechanisms of dynamic cell membrane remodeling. *Nature*, **438**, 590–596.
66. Li, M., Xiao, X., Zhang, W., Liu, L., Xi, N., and Wang, Y. (2014) Nanoscale distribution of CD20 on B-cell lymphoma tumour cells and its potential role in the clinical efficacy of rituximab. *J. Microsc.*, **254**, 19–30.
67. Kenakin, T. (2004) Principles: receptor theory in pharmacology. *Trends Pharmacol. Sci.*, **25**, 186–192.
68. Stephenson, R.P. (1956) A modification of receptor theory. *Br. J. Pharmacol.*, **11**, 379–393.
69. van Meerten, T., van Rijn, R.S., Hol, S., Hagenbeek, A., and Ebeling, S.B. (2006) Complement-induced cell death by rituximab depends on CD20 expression level and acts complementary to antibody-dependent cellular cytotoxicity. *Clin. Cancer Res.*, **12**, 4027–4035.
70. Junttila, M.R. and Sauvage, F.J.D. (2013) Influence of tumour micro-environment heterogeneity on therapeutic response. *Nature*, **501**, 346–354.
71. Rezvani, A.R. and Manoney, D.G. (2011) Rituximab resistance. *Best Pract. Res. Clin. Haematol.*, **24**, 203–216.